Shape optimizations for body-assisted light–matter interactions

Jonas Matuszak,[1] Stefan Yoshi Buhmann,[2] and Robert Bennett[3]

[1] *Physikalisches Institut, Albert-Ludwigs-Universität Freiburg, Hermann-Herder-Str. 3, D-79104 Freiburg i. Br., Germany*
[2] *Institut für Physik, Universität Kassel, Heinrich-Plett-Straße 40, 34132 Kassel, Germany*
[3] *School of Physics & Astronomy, University of Glasgow, Glasgow, G12 8QQ, United Kingdom*

(Dated: June 24, 2022)

We implement a shape optimization algorithm for body-assisted light–matter interactions described by the formalism of macroscopic quantum electrodynamics. The approach uses the level-set method to represent and incrementally evolve dielectric environments. Utilizing finite-difference time-domain techniques we demonstrate the ability of the algorithm by optimizing the rate of resonance energy transfer in two dimensions. The resulting geometries enhance the transfer rate by several orders of magnitude.

I. INTRODUCTION

The discovery of photonic and optical designs is usually governed by the symmetry considerations and experience of the engineer. Traditionally one designs a device and then investigates its desired properties, here referred to as 'forward' design. Inverse design takes the opposite approach by specifying the desired properties and then algorithmically determining the designing of the final device. Some of the first applications of optimization algorithms in photonics were genetic algorithms used to minimize the loss in to fiber-to-ridge waveguide connections [1] and gradient based algorithms to improve parameter settings in order to maximize band gaps [2]. With increasing computational power and the development of the adjoint methods in aerodynamics [3], the application of inverse design algorithms now covers a wide variety of areas. In photonics they range from second harmonic generation [4] to on-chip wavelength demultiplexers [5] or the optimization of solar energy conversion [6]. A detailed review of the application in nanophotonics can be found in Ref. [7].

In contrast to forward design, where the geometry and materials of a device uniquely define its electromagnetic properties, the specified properties of the inverse design problem are not guaranteed to have an existing or unique corresponding design. This leads to the task of finding a design which is closest to the desired properties, which is done by maximizing a merit function encoding the desired properties. Inverse design algorithms usually do not find the global maximum, but converge to a design yielding a local maximum, which still outperforms most design found by a forward design approach.

Such techniques from photonics were only recently expanded to virtual-photon mediated processes. The authors of Ref. [8] derived a general formulation of the adjoint optimization methods in the framework of macroscopic quantum electrodynamics. This allows inverse design techniques to be applied to phenomena such as the Casimir [9] and Casimir–Polder forces [10, 11], Van der Waals forces [12], quantum friction [13], resonance energy transfer [14] and more. Two alternative ways of approaching the inverse design algorithm are offered by the formalism. The additive approach taken in Ref. [8] consists of determining the best possible position where to add a small amount of material to the design and thereby iteratively creating an optimized geometry. The approach taken here is the level-set method [15], which consists of gradually changing the surface of an initial shape towards an optimal geometry.

This article is structured as follows. First, the general formulation of the optimization problem in the macroscopic QED framework is discussed and the level-set method is introduced (Sec. II). Section III illuminates the implementation of the optimization algorithm and introduces the phenomenon of resonance energy transfer as an example application. The results of the application are discussed in Sec. IV and an approach for extending this algorithm to meet manufacturing constraints is given in Sec. V, which is followed by a summary and some concluding remarks (Sec. VI).

II. BACKGROUND

In this section we will outline the general formalism of inverse design for processes described within the framework of macroscopic QED. The desired properties of optical devices are usually represented by a merit function F which depends on the $\boldsymbol{E}, \boldsymbol{B}, \boldsymbol{D}$ and $\boldsymbol{H}$ fields. In the formalism of macroscopic QED, these fields are all expressed in terms of the dyadic Green's tensor $\boldsymbol{G}$ [16] which is uniquely defined by the inhomogeneous Helmholtz equation

$$\left[\nabla \times \frac{1}{\mu(\boldsymbol{r},\omega)}\nabla \times -\frac{\omega^2}{c^2}\varepsilon(\boldsymbol{r},\omega)\right]\boldsymbol{G}(\boldsymbol{r},\boldsymbol{s},\omega) = \boldsymbol{\delta}(\boldsymbol{r}-\boldsymbol{s}), \tag{1}$$

where $\mu(\boldsymbol{r},\omega)$ and $\varepsilon(\boldsymbol{r},\omega)$ are the magnetic permeability and electric permittivity, respectively. This tensor describes the field propagation from a source at position $\boldsymbol{s}$ to an observation point $\boldsymbol{r}$, which means it encodes information about the electromagnetic environment's geometry as well as its material response. Noting that F must

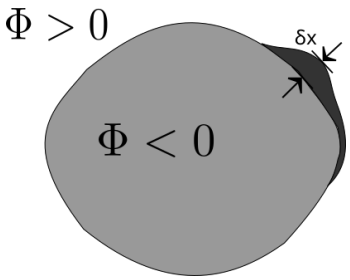

FIG. 1. Level-set method. The shape is deformed by a boundary movement δx.

be an observable we write F as a real-valued functional of $\boldsymbol{G}$:

$$F = \int \mathrm{d}^3 r \int \mathrm{d}^3 s \int_0^\infty \mathrm{d}\omega f[\boldsymbol{G}(\boldsymbol{r}, \boldsymbol{s}, \omega)] \tag{2}$$

By writing F as an integral we can account for spatially extended sources and multimode effects as well as for optimization of effects in extended volumes. As derived in more detail in Ref. [8], a small addition of material results in a change of the merit function:

$$\begin{aligned}\delta F =& \mu_0 \alpha n \int \mathrm{d}^3 r \int \mathrm{d}^3 s \int_V \mathrm{d}r' \int \mathrm{d}\omega \omega^2 \\ &\times 2 \ \mathrm{Re} \left\{ \frac{\partial f}{\partial \boldsymbol{G}}(\boldsymbol{r}, \boldsymbol{s}, \omega) \odot \boldsymbol{G}^T(\boldsymbol{r}', \boldsymbol{r}, \omega) \cdot \boldsymbol{G}(\boldsymbol{r}', \boldsymbol{s}, \omega) \right\}.\end{aligned} \tag{3}$$

This expression allows one to write δF for a material addition at position $\boldsymbol{r}'$ entirely in terms of Green's tensors with sources at $\boldsymbol{r}$ and $\boldsymbol{s}$ (but not $\boldsymbol{r}'$). Calculating the Green's tensors for those two sources is sufficient to know δF at every point $\boldsymbol{r}'$.

The optimization of optical processes can be approached in several ways. One way is to calculate δF over the region of optimization and simply place additional material where the change is highest, which is called the additive approach. Repeating the calculation of δF and placing the new material at the new position of highest change gives the simple iterative optimization algorithm used in Ref. [8]. In this work we take a different approach, the level-set method. We start with an initial geometry and gradually change its boundaries, as sketched in Fig. 1.

The geometry of two different materials can be conveniently represented by a level-set function Φ [15]. The boundary is represented by $\Phi = 0$. Inside the boundary, the level-set function takes negative values and outside it takes positive values. The initial shape of the boundaries is described by

$$\Phi(\boldsymbol{r}(t), t) = 0, \tag{4}$$

where the artificial 'time' parameter t describing the iterative process is introduced. This parameter is used to keep track of the boundaries and their deformation. The total time derivative of (4) yields

$$\frac{\partial \Phi}{\partial t} + \nabla \Phi \cdot \frac{\partial \boldsymbol{r}}{\partial t} = 0, \tag{5}$$

which is the advection equation well-known from fluid dynamics, describing transport of a substance in a velocity field. Since only movement orthogonal to the boundary is relevant, the equation can be simplified by introducing the scalar velocity field in the normal direction of the boundary v_n:

$$\frac{\partial \Phi}{\partial t} + v_n |\nabla \Phi| = 0 \tag{6}$$

If we now want to evolve the boundaries of the geometry in such a way that F increases, we have to choose an appropriate velocity field. For this we can use the information gained from δF. Where the change in F is positive at a point close to (but outside) the boundary, the velocity should be positive, leading the boundary to deform in such a way that this point becomes included within. To ensure this we can rewrite the integral in (3) over the volume as

$$\int_V \mathrm{d}^3 r' \to \int_{\partial V} \mathrm{d}A \delta x(\boldsymbol{r}') = \int_{\partial V} \mathrm{d}A v_n \delta t. \tag{7}$$

The infinitesimal change δx of the boundary is replaced by the product of an infinitesimal time step δt and the velocity normal to the boundary v_n. By choosing the velocity field to be

$$\begin{aligned}v_n = 2 \ \mathrm{Re} \ \alpha n \mu_0 &\int \mathrm{d}^3 r \int \mathrm{d}^3 s \int \mathrm{d}\omega \omega^2 \\ &\times \frac{\partial f}{\partial \boldsymbol{G}}(\boldsymbol{r}, \boldsymbol{s}, \omega) \odot \boldsymbol{G}^T(\boldsymbol{r}', \boldsymbol{r}, \omega) \cdot \boldsymbol{G}(\boldsymbol{r}', \boldsymbol{s}, \omega),\end{aligned} \tag{8}$$

we ensure a positive change of the merit function for small time steps δt:

$$\delta F = \int_{\partial V} \mathrm{d}A v_n^2 \delta t \tag{9}$$

With this we have arrived at a general expression to calculate changes in merit functions which are expressible in terms of the Green's tensor.

Before proceeding, we caution about one complication that has not been taken into account in the above analysis. While the parallel component of $\boldsymbol{G}$ is continuous across an interface, continuity of the product $\varepsilon \boldsymbol{G}$ holds for the perpendicular component (in exactly the same way as the perpendicular component of electric displacement $\boldsymbol{D}$ is continuous across an interface). This could lead to a situation where using a large value of ε causes a point which was outside the interface before optimization to have a significantly different $\boldsymbol{G}$ if the boundary deforms so as to include it. This would entail taking higher-order terms in the Born series that leads to Eq. (3) to ensure convergence [17]. In this work we simply note that the atoms themselves are far enough away from any surface for this problem to have any effect, so while there are imperfections in the optimization algorithm the RET rate calculated for the resulting structures is reliable.

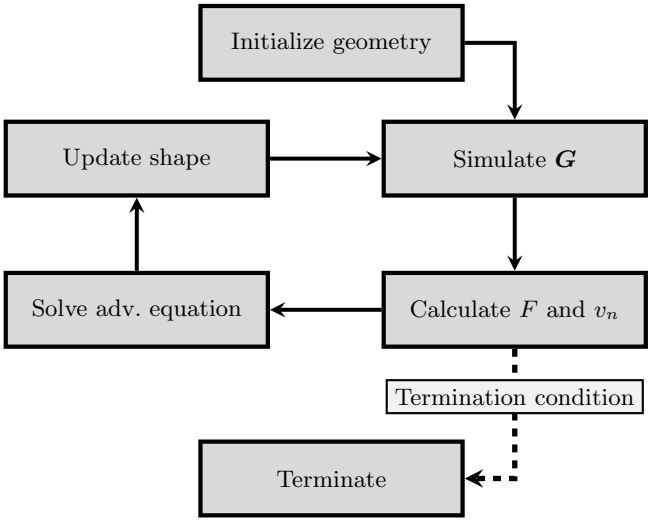

FIG. 2. Flow chart of the inverse design algorithm. It starts with an initial geometry and then calculates $\boldsymbol{G}$ from simulations with MEEP. Using $\boldsymbol{G}$, the merit function and the velocity field v_n are obtained and the latter is used in the advection equation, which is solved for a short time step t. With the new geometry a simulation is started and the process repeats. Under a condition, e.g. a vanishing increase in F, the process is terminated.

III. LEVEL-SET ALGORITHM

We implement the level-set method as indicated by Fig. 2. One starts by choosing an initial geometry as an input to the algorithm, which one encodes in the level-set function Φ. Usually Φ is chosen to be the signed distance function from the shape boundaries.

Next the Green's tensor has to be computed. As seen in Eqs. (8) and (9) computing $\boldsymbol{G}$ for both a source located at $\boldsymbol{s}$ and $\boldsymbol{r}$ is sufficient to know the change in the merit function for a material addition at any point $\boldsymbol{r}'$ in the optimization domain. With the aid of the Green's tensors, the velocity field v_n is obtained and used in the next step to evolve the boundaries of the level set function by solving the advection equation (6) for a short time step t. This results in a small deformation of the original shape leading to an increase in F. The next step is to update the material geometry in the simulation according to the evolved level set function. Here the process repeats and the best shape deformation is calculated for the new geometry. This process can be terminated after a certain amount of iterations or when the merit function no longer increases.

A. Computational Approach

The Green's tensor is known in analytical form only for a few highly symmetric geometries. Here we will encounter arbitrary shapes, which is why we will use a numerical approach. We use existing electrodynamics simulation software, here the open source package MEEP [18], which uses finite-difference time-domain methods, and extract information about $\boldsymbol{G}$ from the electric field.

As discussed in [8], we can relate the Fourier transform of the E-field directly to the Green's tensor and a source current $\underline{\boldsymbol{j}}$. For a point current source $\underline{\boldsymbol{j}}(\boldsymbol{r}',\omega) = \delta(\boldsymbol{r}' - \boldsymbol{s})\underline{\boldsymbol{j}}(\omega)$ we have

$$\underline{\boldsymbol{E}}(\boldsymbol{r},\omega) = \mathrm{i}\mu_0\omega\boldsymbol{G}(\boldsymbol{r},\boldsymbol{s},\omega)\cdot\underline{\boldsymbol{j}}(\omega). \tag{10}$$

By rearranging, a given component of $\boldsymbol{G}$ can be calculated with the simulated fields and the Fourier transformed point current source:

$$G_{ij}(\boldsymbol{r},\boldsymbol{s},\omega) = \frac{\underline{E}_i(\boldsymbol{r},\omega)}{\mathrm{i}\mu_0\omega\underline{j}_j(\omega)}. \tag{11}$$

MEEP provides a built-in Gaussian-shaped source current

$$\boldsymbol{j}(t) = \boldsymbol{j}_0\exp\Big\{-2\pi\mathrm{i}ft - \frac{(t-t_0)^2}{2w^2}\Big\}, \tag{12}$$

with frequency f, time of maximal amplitude t_0 and width w. For the simulation the time of maximal amplitude is set to be five times the temporal width of the Gaussian. Furthermore, a cutoff to the fields is applied after the Gaussian has decayed for five widths.

The advection equation (6) must also be solved numerically. For this we use the finite volume solver for partial differential equations FiPy [19] which incorporates a second-order upwind scheme.

B. Resonance energy transfer

Here we will apply the algorithm as described above to the process of resonance energy transfer [20, 21]. RET consists of two atoms interacting through virtual photon exchange. An initially excited donor atom emits a photon which is absorbed by the acceptor atom in the ground state. This can be well approximated as a single-frequency phenomenon where we also use the dipole approximation to model the donor and acceptor. In order to apply this algorithm to RET we have to express the change in the transfer rate by the means of a merit function. For an acceptor and donor dipole moment $\boldsymbol{d}_\mathrm{A}$ and $\boldsymbol{d}_\mathrm{D}$ the expression is well known as

$$\Gamma = \frac{2\pi\mu_0^2\omega_\mathrm{D}^4}{\hbar}|\boldsymbol{d}_\mathrm{A}^*\cdot\boldsymbol{G}(\boldsymbol{r}_\mathrm{A},\boldsymbol{r}_\mathrm{D},\omega_\mathrm{D})\cdot\boldsymbol{d}_\mathrm{D}|^2. \tag{13}$$

This is already expressed in terms of the Green's tensor, so we can assign the merit function F to be equal to Γ. It is easy to see that the choice

$$f = \frac{2\pi\mu_0^2\omega^4}{\hbar}|\boldsymbol{d}_\mathrm{A}^*\cdot\boldsymbol{G}(\boldsymbol{r},\boldsymbol{s},\omega)\cdot\boldsymbol{d}_\mathrm{D}|^2 \times\delta(\omega-\omega_\mathrm{D})\delta(\boldsymbol{r}-\boldsymbol{r}_\mathrm{A})\delta(\boldsymbol{s}-\boldsymbol{r}_\mathrm{D}) \tag{14}$$

reproduces the merit function $F = \Gamma$. Using f, we calculate the velocity field which increases F for a small deformation of the shape. According to Eq. (8) and with the use of some algebra v_n becomes

$$v_n(\boldsymbol{r}') = \frac{4\pi\alpha n \mu_0^3 \omega_\mathrm{D}^6}{\hbar} \,\mathrm{Re}\left\{ \boldsymbol{d}_\mathrm{A} \cdot \boldsymbol{G}^*(\boldsymbol{r}_\mathrm{A}, \boldsymbol{r}_\mathrm{D}, \omega) \cdot \boldsymbol{d}_\mathrm{D}^* \times \left[\boldsymbol{d}_\mathrm{A}^* \cdot \boldsymbol{G}^T(\boldsymbol{r}', \boldsymbol{r}_\mathrm{A}, \omega)\right] \cdot \left[\boldsymbol{G}(\boldsymbol{r}', \boldsymbol{r}_\mathrm{D}, \omega) \cdot \boldsymbol{d}_\mathrm{D}\right] \right\}. \tag{15}$$

IV. RESULTS

In order to illustrate our method, we restrict the application to systems with translational invariance along one axis, reducing the computational effort to a two dimensional problem. We apply the algorithm to 2D RET with an initial material distribution shaped as a cylinder. In the following we quantify the optimization by a dimensionless ratio Q

$$Q = \frac{\Gamma}{\Gamma_0}, \tag{16}$$

comparing the RET rate Γ of a geometry to the free space rate Γ_0, broadly analogous to the Purcell factor of spontaneous emission.

The transition wavelength is set to 2 µm, the dipoles are aligned along the x-axis and the simulation is run for 300 iterations. The convergence of the algorithm is discussed in App. A. In Fig. 3, the results of the optimization process are shown at four iteration steps ranging from the initial shape to the iteration of highest optimization. The highest optimization is reached with a Purcell factor of approximately $Q = 7 \cdot 10^5$ at the 278^{th} iteration. Within the first iterations the shape grew mainly in its width towards the dipoles and later developed 'arm'–like structures around the dipoles, since the impact of matter placed is higher for small distances to the dipoles. In the direction of dipole alignment the arm structures are open, which can be explained by much weaker radiation in this direction compared to the perpendicular direction. After the development of the first arm structure, a second pair of arms evolved, with a distance of approximately 1 µm at the far end of the shape towards 0.5 µm at their origin, which corresponds to half and a quarter of the transition wavelength respectively. This double arm structure is reminiscent of a waveguide, focusing the electromagnetic radiation from the donor dipole to the acceptor dipole.

Next we apply the inverse design algorithm with the same settings to the initial shapes of a vertical wall and a waveguide (Fig. 4). The optimization for the shapes is of the same order of magnitude with $Q \approx 10^4$. As with the cylinder, the initial wall is modified by the appearance of arm structures, but due to the larger distance of the dipoles to the material, the algorithm lets the shape

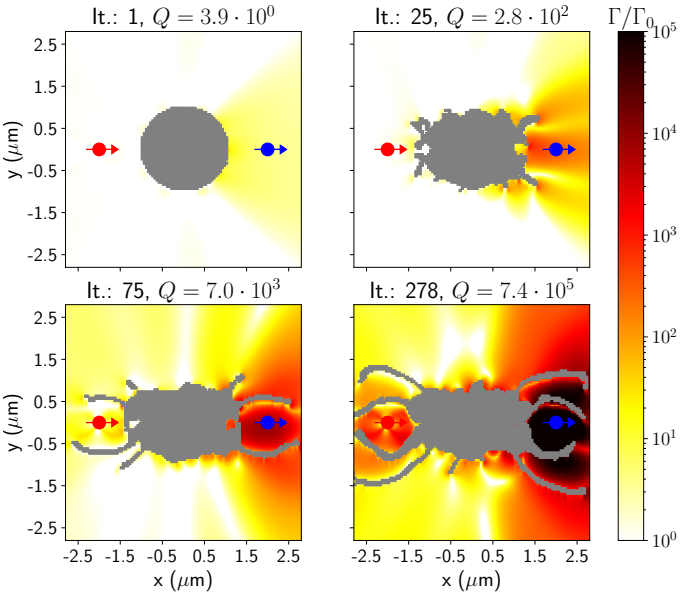

FIG. 3. Inverse design process for 2D RET with the initial shape of a cylinder. The upper left panel shows the initial shape, the red dot is the donor dipole, the blue dot is the acceptor. The arrow through each dot shows the dipole orientation, here they are aligned in the x direction. The simulations are carried out with a resolution of 20 pixels per µm and the time interval t of the evolution of Φ is chosen in such a way, that the boundary moves maximally 0.1 µm (stepsize) per iteration. The evolution of the shape is shown by the iteration steps 25 and 75 and the step of highest optimization, with $Q \approx 7 \cdot 10^5$.

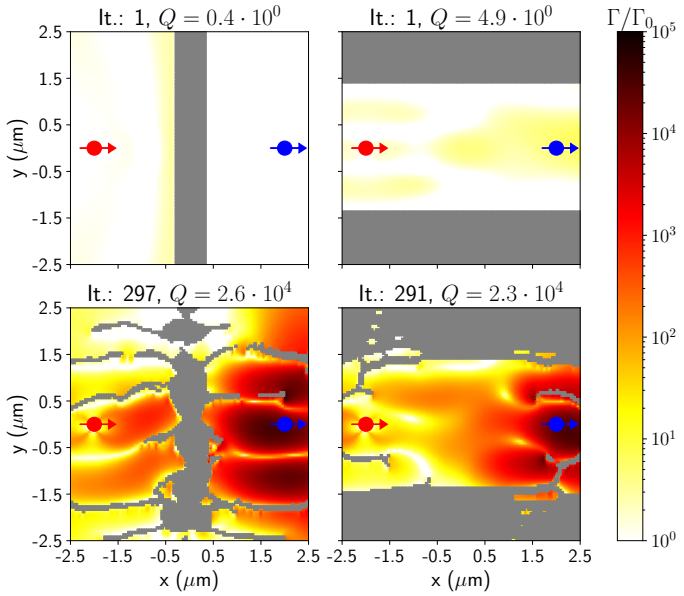

FIG. 4. Results of the optimization for different initial shapes. The first column shows the result of starting with a vertical wall between the dipoles, the second shows the result for a waveguide like structure. The first row shows the initial shapes, the second shows the iteration of the highest amplification for the processes.

first develop waveguide structures above and below the dipoles which are parallel to the dipole orientation and with a width of half the transition wavelength.

The initial waveguide shape also develops arm structures along the dipoles, but in contrast to the other shapes the algorithm places no material between the dipoles. This can be explained by the dipole orientation along the x-axis. The dipole radiation in this direction is weak compared with radiation perpendicular to the orientation, which also results in a stronger deformation of the initial structure above and below the dipoles. Above the donor dipoles small cavities are visible which are periodic in half the transition wavelength in material $\lambda' = \lambda/\sqrt{\varepsilon} \approx 0.58\,\mu\text{m}$. We interpret these as having the same functionality as a Bragg mirror, reflecting radiation efficiently back into the initial waveguide structure.

We also want compare the shape optimization method to the additive method used in [8]. With the additive method the authors achieved a optimization of $Q \approx 10^5$ within 250 iteration steps. The shape optimization algorithm achieved similar optimization of $Q \approx 7 \cdot 10^5$ after 278 iteration steps as seen in Fig. 3, while other shapes stay an order of magnitude below that (Fig. 4). So, depending on the choice of the initial shape, the performance of the two methods is quite similar.

The main qualitative features of the emerging structures are also comparable. For both methods we see thin arm-like structures evolving (see Fig. 5 in [8]). However, the two algorithms also lead to intrinsic structural differences.The additive method places new material at the point of highest impact, which results in a more material–efficient optimization. However the shapes created are also disconnected which may not be feasible to manufacture. With the shape optimization approach we mostly end up with continuous structures. With the shape optimization approach it is also possible to impose manufacturing constraints, since one has a direct representation of the shape in form of the level-set function on which one can place restrictions. One possible constraint will be discussed in Sec. V. The level-set method adds the computational cost of solving the advection equation, however compared to the calculation of the Green's tensor it only adds 5% of additional computation time in our implementation.

A. Rotating Dipoles

The case of rotating dipoles has been brought into focus by recent predictions of effects such as lateral interatomic forces and asymmetric emission [22–25]. In order to observe such phenomena, it may be useful to consider optimized environments for them. For this reason, we apply the algorithm to co- and counter-rotating dipoles. Similarly to circular polarized light we describe them as complex valued vectors. A dipole rotating in the xy plane becomes $\boldsymbol{d} = (1, \mathrm{i}, 0)^{\mathrm{T}}$ and a dipole counter-rotating with respect to $\boldsymbol{d}$ reads $\boldsymbol{d}' = (1, -\mathrm{i}, 0)^{\mathrm{T}}$. Fig. 5 shows the velocity field for the co- and counter-rotating dipoles in the case of free space and the 75th iteration as well as the iteration with the highest Q. The velocity fields are now no longer symmetric along the x-axis and the spiral velocity field of the counter-rotating also does not show symmetry along the y-axis. The highest increase for matter placement in the free space case for the co-rotating dipoles would be below the x-axis, whereas the increase for the counter-rotating dipoles is rotated around the coordinate origin.

These changes are reflected in the evolving shapes. The shape of the co-rotating dipoles develops structures faster at the lower bar, while the shape of the counter-rotating dipoles encloses the donor dipole from below and the acceptor dipole from above, following the distribution of increase in the free space velocity field. The optimization of the magnitude of 10^3 for both rotations is considerably lower than for the shapes with linearly polarized dipoles (which achieved a order of magnitude higher optimizations).

V. ALGORITHM EXTENSIONS

The algorithm can be extended in order to fulfill manufacturing constraints on the material or shapes. We demonstrate this by constraining the curvature of the evolving shape.

In Ref. [26] a technique was introduced where the level-set function is evolved separately with a velocity field proportional to its curvature:

$$\kappa = \nabla \cdot \left(\frac{\nabla \Phi}{|\nabla \Phi|} \right) \tag{17}$$

A weighting function was introduced in order to specify a maximal curvature κ_0 below which the velocity field is set to zero.

$$b(\kappa) = \begin{cases} \kappa & \text{for } |\kappa| > \kappa_0 \\ 0 & \text{otherwise} \end{cases} \tag{18}$$

By evolving Φ with the velocity field $v_\kappa = -b(\kappa)\kappa$ to its steady state, all features with a curvature above κ_0 are eliminated.

Our approach is similar, however we use a localized velocity field v_Γ which only acts in the neighborhood of the surface instead of on the whole level–set function. We choose v_Γ to be proportional and opposite to the curvature of Φ

$$v_\Gamma = -\tau \kappa G(\boldsymbol{d}), \tag{19}$$

where τ is a factor to scale the velocity field and a Gaussian is used to localize this velocity on the surface

$$G(\boldsymbol{d}) = \exp\left\{ \frac{|\boldsymbol{d}|^2}{\sigma} \right\}. \tag{20}$$

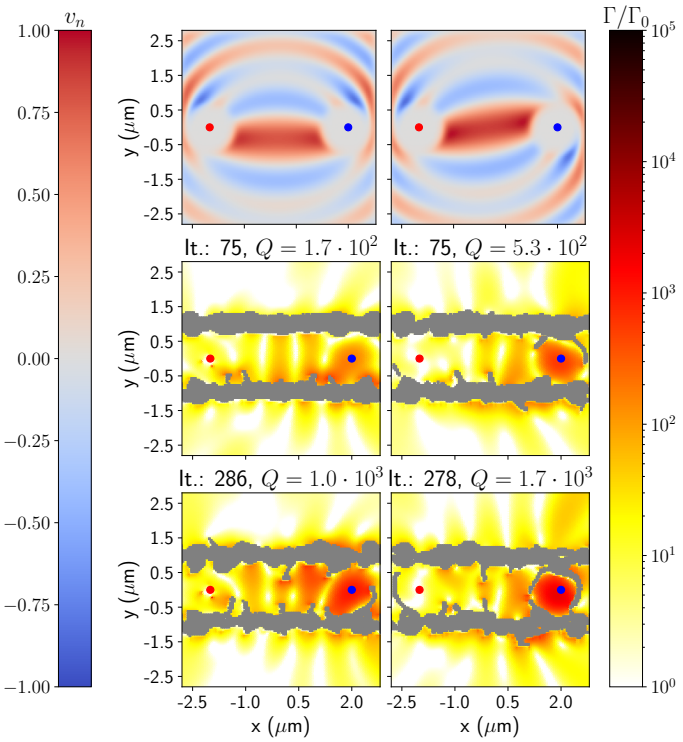

FIG. 5. Optimization results for co- (left) and counter-rotating (right) dipoles for the initial shape of two bars above and below the dipoles. The simulations were run with a resolution of 20 pixels per µm, a transition wavelength of 2 µm and a permittivity of the material of $\varepsilon = 12$. In the upper panels v_n is shown for free space for co- and counter-rotating dipoles respectively. The velocity fields show asymmetry along the x-axis for co-rotating and asymmetry along the x- and y-axis for the counter-rotating dipole. The two white circles are the positions of the dipoles where the velocity was set to zero by hand. The second row shows the shapes after 75 iterations, the third for the iteration of highest optimization, which is of the order of 10^3 for both dipole rotations.

Here $\boldsymbol{d}$ is the shortest distance to the surface and σ is set to a value, such that the Gaussian's width covers a few pixels. Now the advection equation is solved for the velocity $v_t = v_n + v_\Gamma$.

In Fig. 6 the results of this extension applied to the initial shape of a cylinder are shown. We have normalized the additional velocity field in such a way, that the maximal value amounted to $v_{\Gamma,max} = 0.1, 0.8, 1$ and $v_{\Gamma,max} = -0.2$. For the last value we inverted the direction of the velocity field to see the effects of enhancing the curvature of the shape. It can be observed that the thin structures yielding a high contribution to the surface decrease with increasing $v_{\Gamma,max}$, where as for the negative $v_{\Gamma,max}$ the surface is being maximized by the emergence of hole structures. Generally we can see that the optimization is of the order of 10^2 which is three orders of magnitude lower than for the freely evolving shapes.

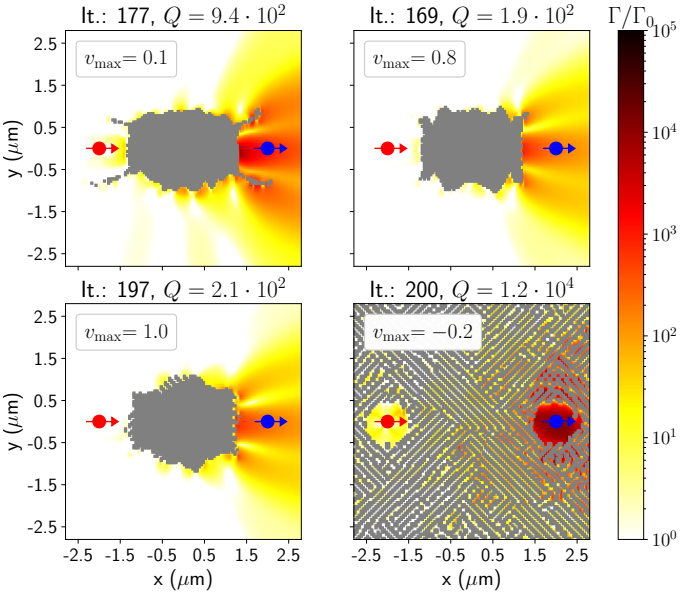

FIG. 6. Results of the optimization algorithm with the initial shape of an cylinder and surface tension term in the velocity field. The velocity contribution from the surface tension is scaled so that its maximal value ranges from 0.1, 0.8 to 1.0 in the first 3 plots. In the lower right plot the contribution is inverted, such that the curvature is enhanced.

VI. CONCLUSION

In this work we have implemented an efficient shape optimization algorithm using the level–set and adjoint methods. The example application to two dimensional resonance energy transfer for different initial structures has yielded shapes with optimizations of several orders of magnitude in the transfer rate. We also demonstrated an example of how the algorithm can be extended to meet manufacturing constraints by restricting the curvature of the optimized shape. Since the method is based on the dyadic Green's tensor it can be applied to a vast variety of other processes and interactions characterizeable by this tensor. Further work could include three dimensional shape optimizations, applications to other processes and implementations of different manufacturing constraints.

Appendix A: Algorithm Convergence

We will briefly investigate the convergence of the algorithm towards a locally optimal design. The accuracy of the simulations with MEEP are mainly determined by their resolution, which is also true for the solving of the advection equation. A second influence on the algorithm is the volume of material added per iteration.

1. Resolution Dependence

To test the convergence of the algorithm depending on the simulation resolution we ran simulations with resolutions ranging from 10 pixels per µm up to 40 pixels per µm. As an initial shape we chose a cylinder of radius $R = 1\,\mu\text{m}$, a simulation size of $7 \times 7\,\mu\text{m}^2$, a transition wavelength of $\lambda = 2\,\mu\text{m}$, the dipole orientations along the x-axis and a maximal change of the border position of $0.1\,\mu\text{m}$ per iteration. The dipole separation is $4\,\mu\text{m}$ and the material has an permittivity of $\varepsilon = 12$. The processes were run for 500 iterations for which the evolution of the Purcell factor Q is shown in Fig. 7.

The Q factors for resolutions of 20, 30 and 40 pixels per µm show very similar behavior, they rise four orders of magnitude within the first 100 iterations and then continue to rise to the order of $Q \approx 10^5$ within the next 400 iteration steps. Here the optimization shows oscillations which become more dramatic with lower resolutions. In the regime of high optimizations the necessary adjustments of the shapes towards an increased optimization are smaller than in the beginning. The processes with lower resolutions overstep the best amount of change, generating larger oscillations, whereas less coarse resolutions allow for a finer adjustment to the velocity field. The lowest tested resolution of 10 pixels per µm rises slower than the other processes and reaches a plateau at an optimization of $Q \approx 10^4$. With lower resolution the volume of the pixelwise addition of material increases, which stretches the limits of the Born approximation, giving another reason for the increase of the oscillations with lower resolution. This resolution is too low to produce optimal results, while the resolutions from 20 pixels per µm seem suitable for the simulations.

2. Stepsize Dependence

Next we investigate the dependence of Q on the magnitude of the boundary deformation, here referred to as the step size. Since we normalize the velocity field such that its maximal value is 1, we control the step size via the time for which Φ is evolved by the advection equation. We again use the initial cylinder shape and the same parameters as before. The resolution was set to be 20 pixels per µm and optimizations were performed with a step size between 0.025 and 0.25 µm per iteration. The results are shown in Fig. 8. Here we see that all processes reached the same order of magnitude for the enhancement, around $Q = 10^5$, except for the smallest step size. Similar to the resolution dependence, Q rises for the three largest step sizes at least four orders of magnitude within the first 100 iterations, while the Purcell factor of the smallest step size reaches this optimization after 100 more iterations. Since the step size is directly related to the amount of matter added per iteration, the Purcell factor for optimizations with larger step sizes rises more quickly. The oscillations which appear after the Purcell factor reaches the order magnitude of 10^4 also increase with the step size. As mentioned in the App. A 1 this is related to the finer adjustment to the given velocity field, for the smallest step size these oscillations are considerably smaller and less frequent. Another reason for the emergence of the oscillation is that we force the shape through normalization of the velocity field to evolve by the set step size. Here the algorithm is forced to change the boundaries, even if the optimal change in the boundary position is smaller than the size of a single pixel.
We conclude that the algorithm reaches higher optimizations faster the larger the step size, but introduces larger fluctuations in the Purcell factor between iteration steps. All of the tested step sizes eventually lead to the same order of magnitude of optimization, except the smallest of 0.025 µm.

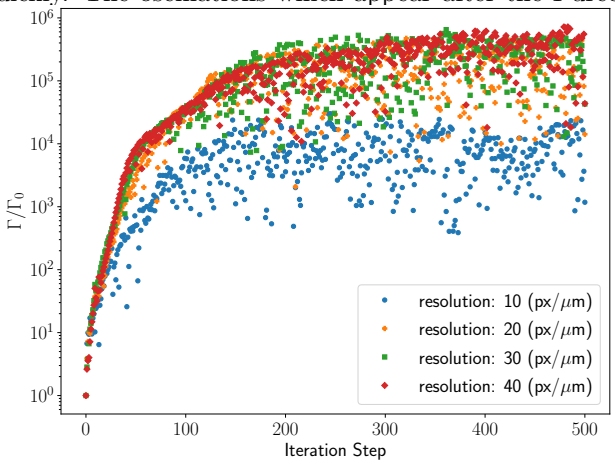

FIG. 7. Resolution dependence on the convergence of the Purcell factor Q. The simulations were performed with an initial shape of a cylinder and a wavelength of 2 µm. The resolution is given in pixel per µm. The inverse design processes perform similarly with the exception of the process with a resolution of 10 pixels per µm. The oscillations in the Purcell factor become prominent in the last 400 iteration steps and increase with lower resolutions.

[1] M. Spuhler, B. Offrein, G.-L. Bona, R. Germann, I. Massarek, and D. Erni, Lightwave Technology **16**, 1680 (1998).

[2] S. J. Cox and D. C. Dobson, SIAM Journal on Applied Mathematics **59**, 2108 (1999).

[3] A. Jameson, Journal of Scientific Computing **3**, 233 (1988).

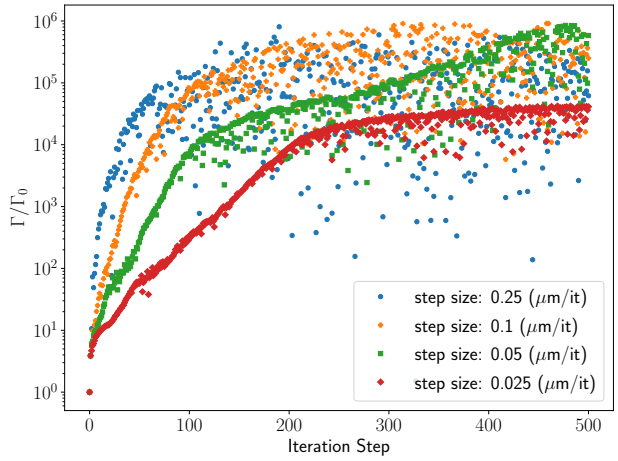

FIG. 8. Dependence of Q on the evolution time of the advection equation. A step size of 0.5 corresponds to an evolution time which lets the boundary move maximally 0.5 pixels per iteration. The processes with the presented step sizes all converge to a Q factor of the same order of magnitude. Smaller step sizes generally take more iteration steps to reach an optimal design but show less oscillations in Q. Larger step sizes converge within fewer steps, but show large oscillations in Q.

[4] Z. Lin, X. Liang, M. Lončar, S. G. Johnson, and A. W. Rodriguez, Optica **3**, 233 (2016).
[5] A. Y. Piggott, J. Lu, K. G. Lagoudakis, J. Petykiewicz, T. M. Babinec, and J. Vučković, Nature Photonics **9**, 374 (2015).
[6] H. Alaeian, A. C. Atre, and J. A. Dionne, Journal of Optics **14**, 024006 (2012).
[7] S. Molesky, Z. Lin, A. Y. Piggott, W. Jin, J. Vucković, and A. W. Rodriguez, Nature Photonics **12**, 659 (2018).
[8] R. Bennett and S. Y. Buhmann, New Journal of Physics **22**, 093014 (2020).
[9] C. Raabe, L. Knöll, and D.-G. Welsch, Physical Review A **68** (2003).
[10] H. B. G. Casimir and D. Polder, Physical Review **73**, 360 (1948).
[11] S. Y. Buhmann, L. Knöll, D.-G. Welsch, and H. T. Dung, Physical Review A **70** (2004).
[12] S. Y. Buhmann, H. T. Dung, and D.-G. Welsch, Journal of Optics B: Quantum and Semiclassical Optics **6**, S127 (2004).
[13] J. Klatt, M. B. Farías, D. A. R. Dalvit, and S. Y. Buhmann, Physical Review A **95** (2017).
[14] T. Förster, Annalen der Physik **437**, 55 (1948).
[15] S. Osher and J. A. Sethian, Journal of Computational Physics **79**, 12 (1988).
[16] T. Gruner and D.-G. Welsch, Physical Review A **53**, 1818 (1996).
[17] S. G. Johnson, M. Ibanescu, M. A. Skorobogatiy, O. Weisberg, J. D. Joannopoulos, and Y. Fink, Phys. Rev. E **65**, 066611 (2002).
[18] A. Oskooi, D. Roundy, M. Ibanescu, P. Bermel, J. Joannopoulos, and S. Johnson, Computer Physics Communications **181**, 687 (2010).
[19] J. E. Guyer, D. Wheeler, and J. A. Warren, Computing in Science & Engineering **11**, 6 (2009).
[20] H. T. Dung, L. Knöll, and D.-G. Welsch, Physical Review A **65**, 043813 (2002).
[21] J. L. Hemmerich, R. Bennett, and S. Y. Buhmann, Nature Communications **9** (2018).
[22] P. Barcellona, R. Bennett, and S. Y. Buhmann, Phys. Rev. A **102**, 020802 (2020).
[23] F. J. Rodríguez-Fortuño, G. Marino, P. Ginzburg, D. O'Connor, A. Martínez, G. A. Wurtz, and A. V. Zayats, Science **340**, 328 (2013).
[24] F. Le Kien and A. Rauschenbeutel, Phys. Rev. A **93**, 043828 (2016).
[25] A. Manjavacas, F. J. Rodríguez-Fortuño, F. J. García de Abajo, and A. V. Zayats, Phys. Rev. Lett. **118**, 133605 (2017).
[26] A. Y. Piggott, J. Petykiewicz, L. Su, and J. Vučković, Scientific Reports **7** (2017).